ISSCR

OPEN ACCESS

Kinome-wide shRNA Screen Identifies the Receptor Tyrosine Kinase *AXL* as a Key Regulator for Mesenchymal Glioblastoma Stem-like Cells

Peng Cheng,[1,6] Emma Phillips,[2] Sung-Hak Kim,[1] David Taylor,[1] Thomas Hielscher,[3] Laura Puccio,[2] Anita B. Hjelmeland,[4] Peter Lichter,[2] Ichiro Nakano,[1,5,*] and Violaine Goidts[2,*]

[1]Department of Neurological Surgery, The Ohio State University, Columbus, OH 43210, USA
[2]Division of Molecular Genetics, German Cancer Research Center, Heidelberg 69120, Germany
[3]Division of Biostatistics, German Cancer Research Center, Heidelberg 69120, Germany
[4]Department of Cell, Developmental, and Integrative Biology (CDIB), University of Alabama, Birmingham, AL 35294, USA
[5]James Comprehensive Cancer Center, The Ohio State University, Columbus, OH 43210, USA
[6]Department of Neurosurgery, The First Hospital, China Medical University, Shenyang, Liaoning 110001, China
*Correspondence: ichiro.nakano@osumc.edu (I.N.), v.goidts@dkfz.de (V.G.)
http://dx.doi.org/10.1016/j.stemcr.2015.03.005
This is an open access article under the CC BY-NC-ND license (http://creativecommons.org/licenses/by-nc-nd/4.0/).

SUMMARY

Glioblastoma is a highly lethal cancer for which novel therapeutics are urgently needed. Two distinct subtypes of glioblastoma stem-like cells (GSCs) were recently identified: mesenchymal (MES) and proneural (PN). To identify mechanisms to target the more aggressive MES GSCs, we combined transcriptomic expression analysis and kinome-wide short hairpin RNA screening of MES and PN GSCs. In comparison to PN GSCs, we found significant upregulation and phosphorylation of the receptor tyrosine kinase AXL in MES GSCs. Knockdown of *AXL* significantly decreased MES GSC self-renewal capacity in vitro and inhibited the growth of glioblastoma patient-derived xenografts. Moreover, inhibition of AXL with shRNA or pharmacologic inhibitors also increased cell death significantly more in MES GSCs. Clinically, *AXL* expression was elevated in the MES GBM subtype and significantly correlated with poor prognosis in multiple cancers. In conclusion, we identified AXL as a potential molecular target for novel approaches to treat glioblastoma and other solid cancers.

INTRODUCTION

Glioblastoma (GBM) is the most common primary malignant brain tumor in adults. Despite multimodal aggressive therapies, survival of a vast majority of the patients is less than 2 years with the 5-year survival rate as low as 5% (Stupp et al., 2009). Previous efforts in the development of therapeutics for GBM have largely depended on studies with conventional GBM cell lines. While providing some benefits, genetic and phenotypic drift is inevitable in these long-term in vitro cell cultures. Importantly, the standard GBM cell lines cannot recapitulate the heterogeneous cellular populations of GBM (Ernst et al., 2009; Lee et al., 2006). These limitations may partially explain the large gap between promising in vitro data and disappointing GBM clinical trial outcomes. The identification of effective therapeutics has been hindered, in part, by the lack of more clinically relevant GBM models. Tumor-initiating GBM stem-like cells (GSCs) isolated from patients propagate the heterogeneity of the original GBMs in immunocompromised mice and preserve specific genetic alterations found in the original tumor (Hemmati et al., 2003; Singh et al., 2004).

In the past decade, transcriptomic and methylation analyses have classified GBM tumors into several subtypes (Phillips et al., 2006; Sturm et al., 2012; Verhaak et al., 2010), including proneural (PN), classical, and mesenchymal (MES) GBMs. While these signatures are based on

the predominant gene expression patterns in the tumor and correlate with mutation and epigenetic status, GBMs are very heterogeneous, and data demonstrate the presence of cells of multiple subtypes within a single tumor as well as transitions between subtypes (Bhat et al., 2013; Patel et al., 2014; Piao et al., 2013). Our work has classified the majority of GSCs as MES or PN based on transcriptomic signatures. In comparison to PN GSCs, MES GSCs display highly aggressive and radioresistant phenotypes (Mao et al., 2013). The core MES GSC gene signature also correlates with poor GBM patient prognosis, indicating the importance of understanding molecular mechanisms driving MES-specific biology. These patient-derived and subtype-specific GSCs provide a powerful model for the heterogeneous human disease and future therapy development.

Kinases are often activated in cancer, indicating the potential of kinase inhibitors for cancer therapy. Kinases control a wide variety of cell functions related to tumorigenesis, including survival/apoptosis, cell-cycle progression/proliferation, stem cell maintenance, DNA damage repair, cell motility/invasion, and therapeutic resistance. Indeed, the discovery of oncogenic kinases and development of target-specific inhibitors have already revolutionized the treatment of certain groups of cancers, exemplified by the success of Gleevec for chronic myeloid leukemia (Druker et al., 2001). Protein kinases are now firmly established as a major class of anti-cancer therapeutic targets. There has been an explosion in the number of kinase inhibitors

CrossMark
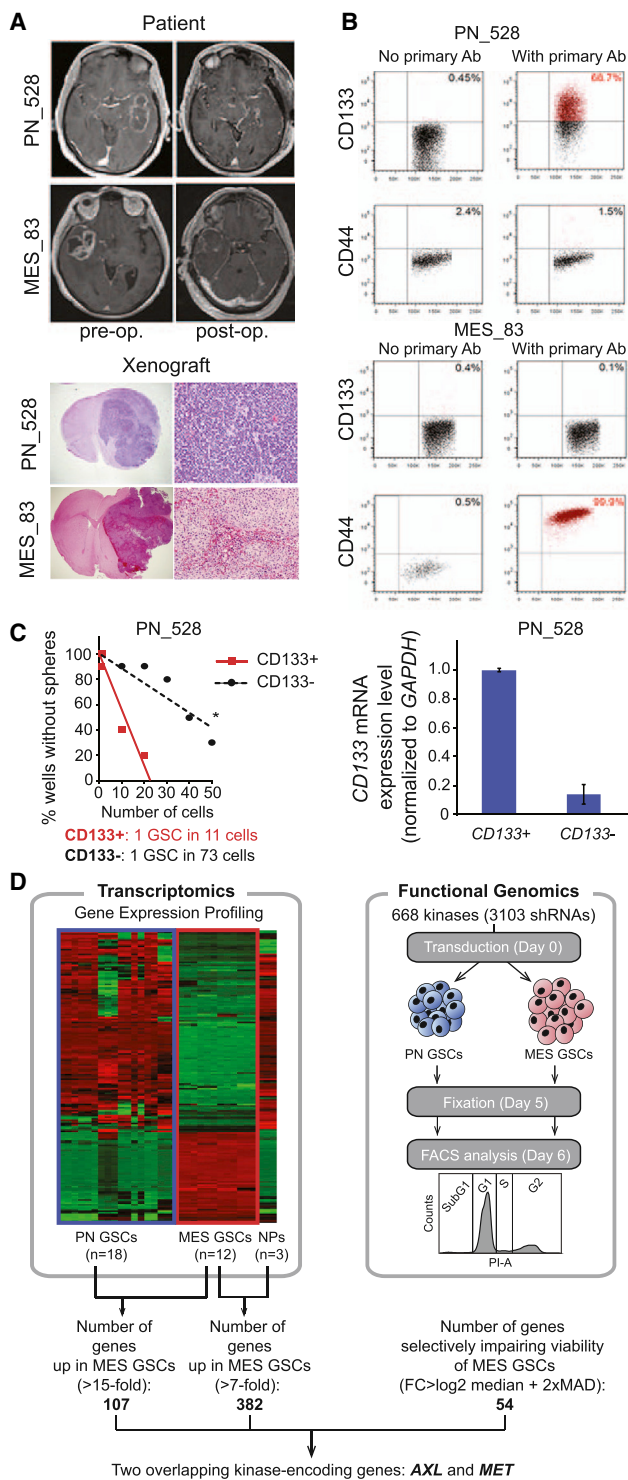
Figure 1. Patient-Derived PN and MES GSCs Used for In Vitro Screening

(A) MRI captions taken pre-operation and post-operation of GBM patients (upper) and H&E staining of the xenotransplanted cells in NOD/SCID mice (lower). Magnification is 20× (left) and 100× (right).

that have successfully entered the clinic or have produced promising data in preclinical drug development pipelines (Zhang et al., 2009). While such success has not yet been achieved for GBM, identification of kinases whose inhibition attenuates GSC properties may pave the way toward novel therapeutics (Mellinghoff et al., 2012).

Here, we sought to identify new druggable therapeutic targets for GBM. We combined transcriptome expression profiling and loss-of-function approaches to identify human kinases that play differential roles in PN and/or MES GSCs. Using a human kinome-wide lentiviral shRNA library, we identified 82 candidates that are essential for the proliferation and viability of MES and/or PN GSC-containing neurosphere cultures in vitro. Among them, 54 specifically regulated MES GSCs, underlining the dependence of these GSC subtypes on differential oncogenic signals. Subsequently, the receptor tyrosine kinases (RTKs) *MET* and *AXL* were the only two genes that were significantly differentially expressed in PN and MES GSCs and the silencing of which caused a significantly different phenotype between PN and MES GSCs. Since an inhibitor against AXL has recently entered phase I clinical trials for hematopoietic malignancy (Holland et al., 2010; Janning et al., 2015), in this study, we decided to characterize *AXL* in GSCs derived from GBM tumors.

RESULTS

Patient-Derived GSCs Display MES or PN Characteristics

The new "omics" data available for GBM suggesting the existence of several subtypes of GBM calls for detailed characterization of the tumor models used in vitro. As previously described (Mao et al., 2013), we successfully isolated GSCs from GBM patients that can readily recapitulate the original tumor's phenotype in vivo (Figure 1A), express GSC cell surface markers (Figure 1B), and are more self-renewing than cells that are CD133 derived from the same tumor (Figure 1C). Supervised clustering using The Cancer Genome Atlas (TCGA) classification of the genome-wide expression profiles obtained from the isolated GSCs

(B) Representative FACS plots demonstrating expression of CD133 and CD44 PN GSCs (PN_528) and in MES GSCs (MES_83).
(C) Neurosphere formation assay of CD133+ versus CD133- PN_528 GBM cells. *CD133* mRNA expression level in sorted cells was verified by qRT-PCR (RT-PCR). Error bars represent the SD from three technical replicates. Stem cell frequency was calculated by ELDA analysis.
(D) Flowchart depicting the experimental procedure used to investigate kinases whose silencing induces cell death or impairs proliferation.
See also Figure S1.

allowed us to classify them as MES or PN. Despite the abundance of data provided, these profiling methods do not yield information on genes that are directly involved in cell fate decisions. To fill this gap, we combined data from the genome-wide transcriptome profiles (Mao et al., 2013) with a loss-of-function screen. Based on the highly aggressive nature of MES GSCs, we specifically sought to identify kinases that (1) impair the viability of MES GSCs upon knockdown and (2) are differentially expressed in MES GSCs in comparison to PN GSCs and neural progenitor cells (NPs) derived from human fetal brains (Miyazaki et al., 2012; Nakano et al., 2011) (Figure 1D).

Identification of Kinases that Impair Both MES and PN GSC Viability and Alter Cell Cycle

In order to identify kinases that induce cell death and/or cell-cycle arrest upon knockdown in GSCs of the PN and/ or MES subtype, we performed a lentiviral-based silencing screen in vitro. We transduced the MES GSC line 83 and the PN GSC line 528 with a subset of the TRC library specifically targeting the human kinome. Using fluorescence-activated cell sorting (FACS) analysis with propidium iodide staining, we simultaneously detected cell death and characterized the different phases of the cell cycle. The significance of cell percentage in the G1, S, and G2 phases of the cell cycle was assessed after subtraction of the SubG1 phase.

Kinases that were equally relevant in both MES and PN GSCs were defined for each cycle phase separately. Analysis was based on normalized data averaged from shRNAs from both cell lines using one-sided adjusted p values ($p < 0.05$) and a threshold of the median fold change (FC) plus two median absolute deviations (MADs). Among the 668 kinases represented in the tested panel, knockdown of 7 kinases significantly increased the percentage of cells in the SubG1 phase in MES and PN GSCs in comparison to non-targeting controls (shNT), including *FYN*, *RIPK3*, and the *RET* kinases (Figure S1A). Another 13 kinases significantly altered the cell cycle by increasing the number of cells entering the S (such as *CARKL*, *EPHA5*, and *MAP4K2*) or the G2 phases (*EGFR* and *DAPK2*) in both MES and PN GSCs (Figure S1B).

Identification of Kinases Specifically Regulating MES or PN GSC Viability

In order to identify kinases that specifically regulate the viability of MES or PN GSCs, ratios of SubG1 cell number for each targeting shRNA to the shNT were calculated. This analysis was based on one-sided adjusted p values ($p < 0.05$) and a threshold of the median FC between PN and MES +2 times the MAD. Several of the identified kinases impaired viability of the MES GSCs only, as indicated by increased percentages of cells in the SubG1 phase of the
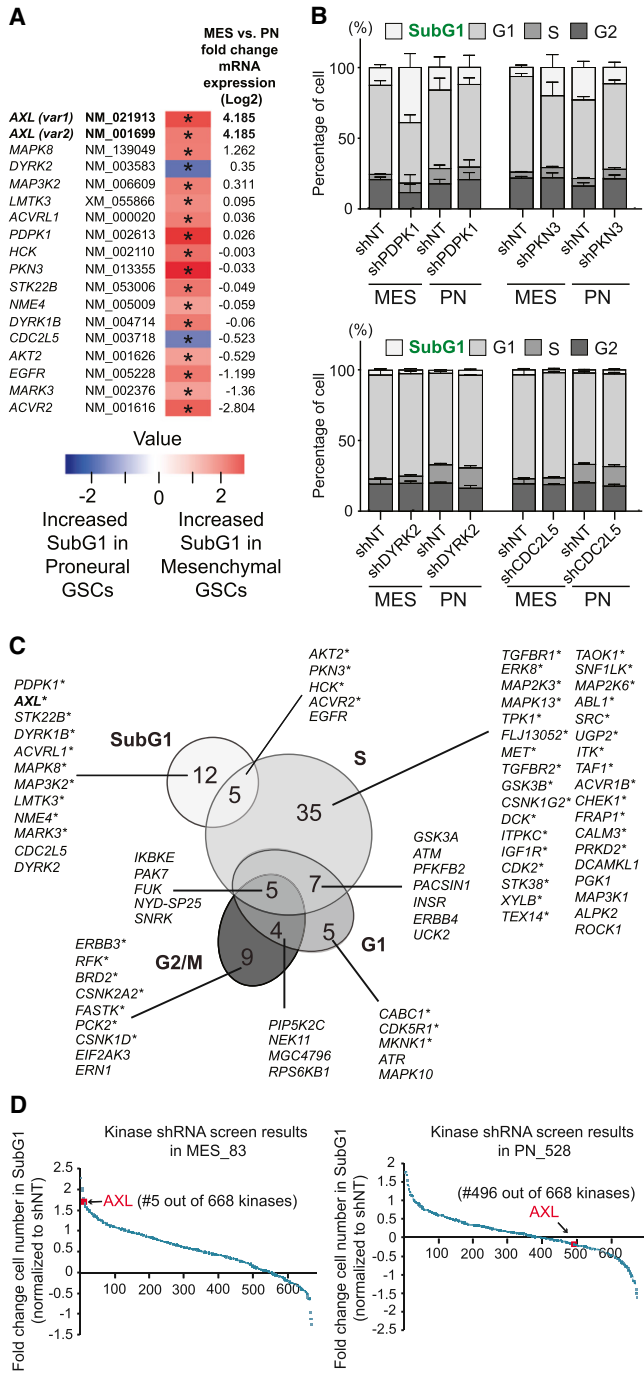
cell cycle (Figure 2A). For example, knockdown of genes such as *PKN3*, *PDPK1*, and *AXL* significantly increased the percentage of SubG1 cells in MES GSCs in comparison to PN GSCs (Figures 2A and 2B). In contrast, targeting *CDC2L5* and *DYRK2* more strongly affected the percentage of SubG1 cells in PN GSCs (Figures 2A and 2B). Of the top three kinase hits in MES GSCs, *AXL* was the only one highly overexpressed in MES GSCs in comparison to PN GSCs at the mRNA level in our microarray analysis (Figure 2A). Therefore, our functional shRNA screen identified targets whose importance would not have been recognized in analysis of gene expression changes alone.

Identification of Kinases Specifically Altering MES or PN GSC Cell Cycle Phase

After assessing the impact of the kinase directed shRNAs on the SubG1 phase, we further analyzed the cell-cycle data to identify kinases that differentially altered the G1, S, or G2 phases in MES or PN GSCs. We identified 70 kinases with specific activity in at least one of these three cell-cycle phases (Figure 2C). Differential cell-cycle effects of kinase directed shRNAs were most prominent in the S phase for MES GSCs, where *GSK3A* and *AKT2* were found to significantly reduce the percentage of dividing cells (Figure S2). In PN GSCs, *ROCK1*, *ALPK2*, and *MAP3K1* had differential S-phase effects. Moreover, the knockdown of certain kinases, such as *IKBKE*, *PAK7*, or *FUK*, resulted in effects on multiple cell-cycle phases, emphasizing the importance of those genes for the proliferation of the targeted GSCs (Figures 2C and S2). To assess the relevance of the identified kinases, we performed a gene ontology analysis using the DAVID bioinformatics resource. As depicted in Figure S3, shRNAs that specifically impaired the MES GSC cell cycle were directed against kinases enriched for known biological processes regulating cell cycle. In contrast, shRNAs specifically altering the PN GSC cell cycle were directed against kinases associated with neurological processes.

A Combination of Transcriptomics and Functional Genomics Identifies AXL

Genome-wide mRNA expression profiling was performed on GBM neurosphere lines each cultivated from six PN and four MES high-grade glioma patients in triplicate (Mao et al., 2013). Genes that showed an increase of mRNA expression in MES GSCs of >15-fold as compared with PN GSCs were designated as MES specific. To assess the specificity of the gene expression for GSCs in comparison to non-neoplastic NPs, three independent cultures from a normal NP line were included in the analysis. We selected candidate genes with mRNA expression >7-fold higher in MES GSCs compared with the NPs. In order to identify genes that selectively impair the viability of MES GSCs, we compared the list of identified genes based on

A

MES vs. PN fold change mRNA expression (Log2)

Gene	Accession		Value
AXL (var1)	NM_021913	*	4.185
AXL (var2)	NM_001699	*	4.185
MAPK8	NM_139049	*	1.262
DYRK2	NM_003583	*	0.35
MAP3K2	NM_006609	*	0.311
LMTK3	XM_055866	*	0.095
ACVRL1	NM_000020	*	0.036
PDPK1	NM_002613	*	0.026
HCK	NM_002110	*	-0.003
PKN3	NM_013355	*	-0.033
STK22B	NM_053006	*	-0.049
NME4	NM_005009	*	-0.059
DYRK1B	NM_004714	*	-0.06
CDC2L5	NM_003718	*	-0.523
AKT2	NM_001626	*	-0.529
EGFR	NM_005228	*	-1.199
MARK3	NM_002376	*	-1.36
ACVR2	NM_001616	*	-2.804

-2 0 2
Increased SubG1 in Proneural GSCs — Increased SubG1 in Mesenchymal GSCs

D

Kinase shRNA screen results in MES_83 — AXL (#5 out of 668 kinases)

Kinase shRNA screen results in PN_528 — (#496 out of 668 kinases) AXL

Figure 2. Knockdown of a Subset of Kinases Differentially Induces Cell Death in MES or PN GSCs

(A) List of kinases that induce cell death significantly (*, adjusted p < 0.05) in MES GSCs (red) or in PN GSCs (blue). mRNA expression FC between PN and MES GSCs is indicated on the right side of the heatmap.

(B) Stacked bar charts of the top two genes inducing cell death in MES (above) or in PN (below) GSCs. Average of the shNT used for normalization and the shRNAs targeting the indicated gene is shown. Error bars represent the SD.

(C) Venn diagram grouping kinases whose silencing induces a significant change of the cell-cycle phases specific to MES or to PN GSCs (see also Figures S2 and S3). Asterisks highlight 54 kinases whose silencing altered the cell cycle specifically in MES GSCs.

(D) Ranking of *AXL* according to the cell number FC in SubG1 in MES and PN GSCs. Data are all initially normalized to the non-targeting shRNA.

these transcriptomics data with the ones from the functional genomics screen. The genes encoding the AXL RTK (AXL) and the MET Proto-Oncogene (MET) proteins were the only two genes that appeared in both datasets (Figures 1C, 2A, 2C, and 2D). As recent studies indicate that AXL is a potentially attractive therapeutic target and one of its kinase inhibitors has entered the phase I clinical trial for hematologic malignancy, we focused on AXL for further characterization in GSCs in this study.

AXL Is Highly Expressed in MES but Not PN GSCs

To characterize the pathophysiological role of *AXL* in MES and PN GSCs, we further analyzed the data from the transcriptome microarray (Mao et al., 2013). In these data, including 18 patient-derived PN GSC samples, 12 patient-derived MES GSC samples, 5 astrocyte samples, and 3 normal NPs, all 12 MES GSC samples revealed high expression of *AXL*. In contrast, 18 PN samples showed either undetectable *AXL* expression by microarray analysis or substantially lower expression (Figure 3A). These results were confirmed by qRT-PCR using three PN and three MES GSC samples (Figure 3B). *AXL* expression in MES GSCs was also elevated in comparison to NPs (Figure 3A). Concordant with the mRNA expression, AXL protein expression was increased in MES compared with PN GSCs, as determined via immunoblotting (Figure 3C) and immunofluorescence (Figure 3D). In addition, the phosphorylated form of AXL (pY779) was only detected in MES GSCs (Figures 3C and 3D), suggesting that the AXL pathway is specifically activated in MES but not PN GSCs. Our data are in accordance with other datasets of patient-derived GBM spheres (Figures 3E and 3F; Bhat et al., 2013; De Bacco et al., 2012) and GBM patient specimens (Figures 3G and 3H; Brennan et al., 2013; Sturm et al., 2012). Together, these data demonstrate that AXL is preferentially expressed and activated in MES GBM.

Knockdown of AXL Decreased Clonogenicity of MES GSCs In Vitro

To further confirm the high-throughput screening results indicating that *AXL* shRNA increased the number of SubG1 cells (Figure 4A) and to investigate the function of *AXL* in MES GSCs, we transduced two MES GBM sphere samples (83 and 1123) with two gene-specific shRNAs for *AXL* (shAXL#1 and shAXL#2) and shNT as a control. The

knockdown of AXL protein by the directed shRNAs after transduction was confirmed using immunoblotting (Figure 4B). In vitro growth assays demonstrated that knockdown of *AXL* decreased the growth of 83 and 1123 MES GSCs (Figure 4C) in comparison to the shNT. In vitro limiting dilution assays showed a decreased capacity to form neurospheres in 83 and 1123 GBM upon AXL knockdown, indicating a reduced clonogenicity of the GSCs (Figures 4D and 4E). These observations were concordant with an increase in apoptosis, as demonstrated by significantly higher Caspase 3/7 activity with *AXL* targeting (Figure 4F). As suggested by its expression level, the knockdown of *AXL* in the PN GSC line did not impair clonogenicity (Figure 4E) nor increase apoptosis (Figure 4F). Interestingly, MES GSCs also showed higher sensitivity than the PN_528 GSC line to BGB324, an AXL inhibitor (Figure 4G). Sigmoidal dose-response analysis indicated a lower IC_{50} in the MES versus the PN GSCs tested (IC_{50} of 1.027 and 2.035 μM, respectively). The specificity of BGB324 for AXL was assessed by the level of AXL phosphorylation with and without inhibitor treatment (Figure 4G).

AXL Regulates In Vivo Tumorigenicity of MES GSCs

We next assessed the role of *AXL* in MES GSC tumorigenic potential. To this end, we knocked down AXL in 83 and 1123 GSCs using shALX#2 and used shNT as a control. Transduced cells were orthotopically injected into the striatum of immunocompromised mice. Mice receiving shAXL#2 transduced 83 or 1123 GSCs did not show any signs of tumors 2 weeks after transplantation, whereas mice injected with shNT transduced cells had large GBMs (Figure 5A). Knockdown of *AXL* also significantly increased the survival of mice until the development of neurological signs in comparison to shNT controls (n = 12 with 83 GBM, p = 0.0005, with log-rank test, and n = 10 with 1123 GBM, p = 0.0018, with log-rank test). However, animals that received shAXL-infected 83 or 1123 GSCs developed tumors about a month after transplantation (Figure S4). These results suggest that *AXL* is an important regulator of MES GBM growth, but not absolutely required for tumor initiation.

AXL Expression Correlates with *CD44* Expression and Is Highly Expressed in Glioma Samples

In view of the importance of *AXL* for the viability of GSCs from the MES subtype, we investigated whether *AXL* mRNA expression correlated with the mRNA expression of the MES marker *CD44*. The RNaseq data generated by the TCGA Research Network (http://cancergenome.nih.gov/) showed a significant correlation between the expression of both genes (Figure 6A). Interestingly, the silencing of *AXL* in two MES GSC lines (83 and 1123) decreased the mRNA expression of *CD44* (Figure 6B), suggesting a

co-regulation of both genes. These data were confirmed at the protein level by immunofluorescent staining of orthotopically injected 83 GSCs transduced with shNT or shRNA targeting AXL (shAXL#2) (Figure 6C). Supporting this finding, in orthotopically xenografted tumors derived from patient GSCs, AXL co-expressed with CD44 preferentially in perinecrotic pseudopalisading areas (Figure S5). Moreover, *AXL* and *CD44* co-expression correlated with the clinical survival time of glioma patients. The data generated by TCGA Research Network, visualized using the GBM-Bio Discovery Portal, shows that the co-upregulation of *AXL* and *CD44* is a predictor of poor survival in GBM patients (Figure 7A).

Finally, we assessed the relevance of AXL as a potential therapeutic target for GBM and other tumor entities. Evaluating the Sun et al. (2006) dataset, elevated *AXL* expression was observed in glioma compared with non-tumor (n = 23 non-tumor group; n = 7 grade II astrocytoma; n = 19 grade III astrocytoma; n = 81 GBM group; p < 0.01, p < 0.05, and p < 0.0001, respectively, probeset: 202686_s_at) (Figure 7B). Supporting this expression pattern, we found that AXL was highly expressed in high-grade gliomas, including GBM, but not in normal brain tissues or lower grade gliomas (Figure 7C), as determined by evaluating phospho-AXL immunoreactivities in glioma patient sections. In the GBM samples from the Gravendeel et al. (2009) dataset through the R2 microarray analysis and visualization platform (http://r2.amc.nl), *AXL* expression trended toward poor survival of GBM patients, although the data did not meet statistical significance (Figure 7D; p = 0.060 with log-rank test). In silico analysis of existing datasets for other cancer types, including ovarian, colon, pancreatic, and Burkitt's lymphoma cancer, also linked *AXL* to poor prognosis, although this was not true for every tumor type or dataset (Figures 7E–7H) (Collisson et al., 2011; Hummel et al., 2006; Smith et al., 2010; Tothill et al., 2008). Collectively, these results indicate that AXL is a potential molecular target for anti-cancer therapy.

DISCUSSION

In this study, we took a stepwise approach with transcriptome expression analysis and a functional shRNA screen in order to identify common and differential regulators of PN and MES GSC growth.

AXL is a member of the TAM (TYRO3-, AXL-, MER-TK) subfamily of RTKs (O'Bryan et al., 1991). This family shares structural homology, including a conserved sequence within the kinase domain (Linger et al., 2008). In contrast to little or no expression in normal brain tissue, aberrant *AXL* expression in GBM has been described, raising the possibility that AXL could be an attractive therapeutic
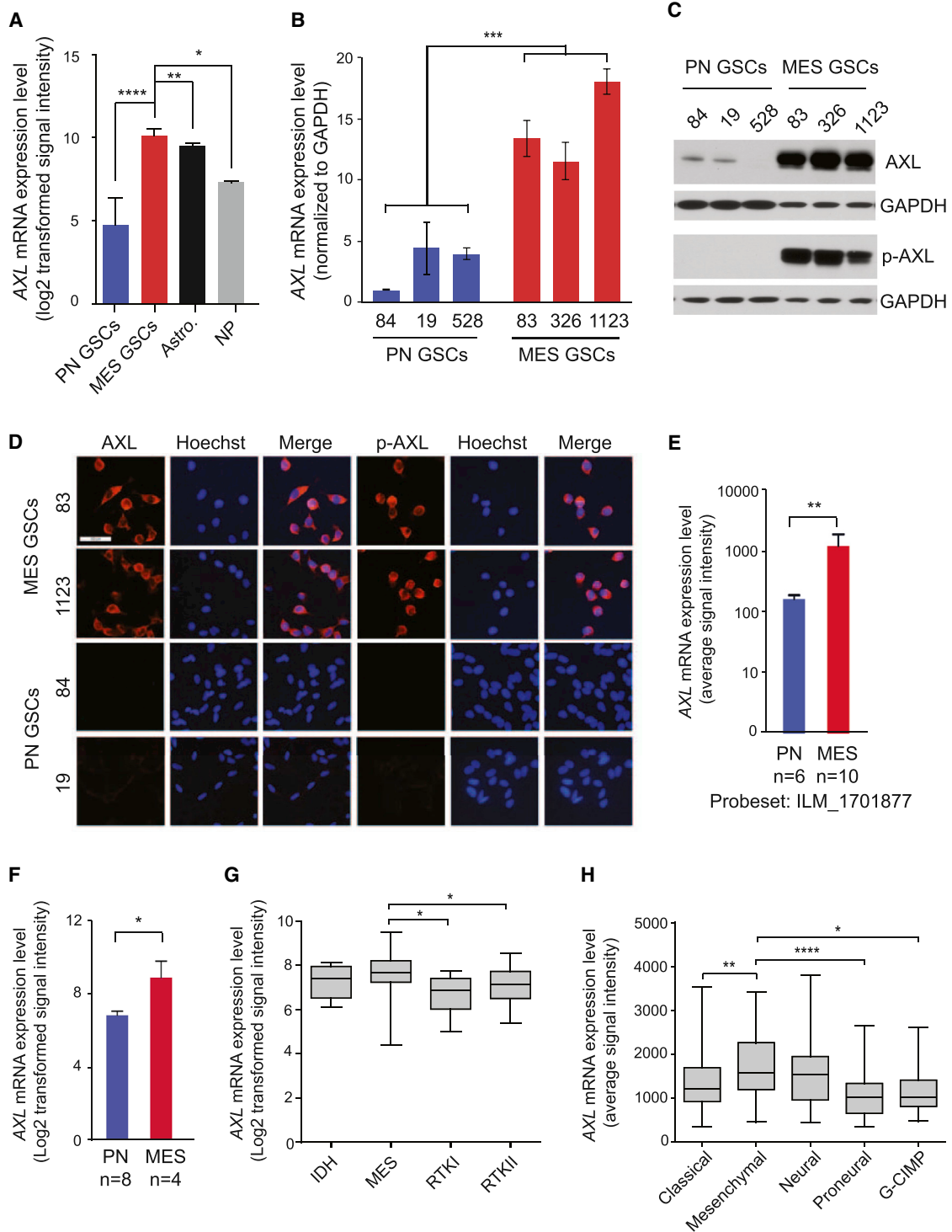
Figure 3. AXL Is More Highly Expressed in MES Than PN GSCs

(A) Microarray analysis of *AXL* mRNA expression in PN GSCs from individual patients (n = 18), MES GSCs (n = 12), astrocytes (n = 5), and neural progenitors (n = 3) (Mao et al., 2013) (*p < 0.05; **p < 0.01; ****p < 0.0001; Mann Whitney t test in comparison to MES GSCs).

(B) *AXL* mRNA expression as determined by qRT-PCR in PN (n = 3) and MES (n = 3) (***p < 0.0001; t test). Error bars represent the SD from three technical replicates.

(legend continued on next page)

target for GBM. Earlier work has established the physiological roles of AXL in glioma cell lines using both in vitro cell culture systems and in vivo xenografted tumor models (Keating et al., 2010; Vajkoczy et al., 2006). Gene-specific knockdown of *AXL* has been shown to induce cell apoptosis, decrease cell proliferation and migration, and improve sensitivity to temozolomide—the current first-line chemotherapy for GBM (Keating et al., 2010; Vajkoczy et al., 2006). Our data demonstrate that a subset of GSCs in GBM tumors—MES but not PN GSCs—is sensitive to *AXL* knockdown both in vitro and in vivo. Supporting these differential sensitivities, a phosphorylated form of AXL is detected only in the MES GSCs. Knubel et al. (2014) recently reported that foretinib treatment hindered tumor growth in a mouse model of GBM using the glioma cell line U251 in vivo. Notably, foretinib is a multikinase inhibitor with the most potent effect on another TAM RTK, MER-TK, with comparable inhibitory effects on AXL, c-Met, and VEFRR2/KDR (Liu et al., 2009; Qian et al., 2009). Several phase II clinical trials with foretinib are in progress, addressing breast, liver, renal, gastric, and other cancers (Choueiri et al., 2013; Liu et al., 2009; Shah et al., 2013). Zhang et al. (2012) recently identified that activation of the AXL kinase is a mechanism by which resistance is acquired to EGFR-targeted tyrosine kinase inhibitors (TKIs) in *EGFR* mutant non-small-cell lung cancers. In some cases, they found that *AXL* upregulation occurs in the context of what appeared to be epithelial to MES transition (EMT) and EMT-associated transcriptional reprogramming, leading to acquired resistance. Vuoriluoto et al. (2011) also reported similar data for AXL-mediated EMT-like changes in breast cancer cells. These studies raise the possibility that secondary molecular events may occur in GBM cells or GSCs that facilitate escape from AXL targeting therapies. For example, AXL inhibition may lead to the activation of other TAM family members such as MerTK and Tyro3. Indeed, TAM family members form heterodimers and cross-talk with each other (Linger et al., 2008). Since they share the common ligand Gas6 and the common downstream signaling pathways PI3K and MAPK, targeting AXL alone may lead to a switch to other TAM family members to persist the acti-

vation of the same ligand-driven oncogenic pathways. Our data illustrate that *AXL* silencing significantly prolongs survival of mice bearing GSC-derived brain tumors, yet eventually these mice die due to tumor burden. As tumors can arise from *AXL*-shRNA-transduced MES GSCs, it will be important to investigate how these tumors escape from AXL inhibition in additional studies. Of note, foretinib treatment reduces growth of U251-derived mouse subcutaneous tumors, whereas when this treatment is discontinued, tumors showed a quick upturn reaching growth rates even more aggressive than naive tumors (Knubel et al., 2014). These studies indicate a risk for advancing malignancy if tumors are treated with AXL inhibition solely. Future studies will need to explore downstream molecular changes after AXL inhibition in GSCs and GSC-derived tumors in order to avoid establishing acquired resistance in GBM patients after AXL-targeted therapies.

In conclusion, our experimental setting allowed the identification of differences in survival and proliferation pathways between PN and MES GSCs. The sensitivity of MES GSCs to the silencing of *AXL* highlights its importance in this subgroup of GSCs and suggests its potential for use as a therapeutic target.

EXPERIMENTAL PROCEDURES

GSC Isolation and Cell Culture

GSC samples were collected at The Ohio State University in accordance with an institutional review board-approved protocol. GSCs were isolated as previously described (Gu et al., 2013; Mao et al., 2013). Neurospheres were cultured in DMEM/F12 (Invitrogen) containing 2% B27 supplement (Invitrogen) (vol/vol), heparin (2.5 µg/ml), basic fibroblast growth factor (bFGF) (Peprotech, 20 ng/ml), and epidermal growth factor (EGF) (Peprotech, 20 ng/ml). bFGF and EGF were added twice a week. The phenotypes of these neurospheres were characterized according to the methods described previously (Guvenc et al., 2013; Jijiwa et al., 2011). All of the neurospheres used in this study were maintained <30 passages. The human fetal neural stem cell sample (16wf) was established at the University of California at Los Angeles as described previously (Miyazaki et al., 2012; Nakano et al., 2011). Astrocytes were derived from fetal

(C) Representative western blot of total AXL and phospho-AXL (pY779) expression in PN (528, 19, and 84) and MES GSCs (83, 326, and 1123).

(D) Representative immunofluorescent images of total AXL and phospho-AXL staining in MES and PN GSCs (scale bar represents 50 µm).

(E and F) mRNA expression of *AXL* as determined by gene expression profiling from previously published datasets: (E) De Bacco et al. (2012) (**$p < 0.01$, unpaired t test) and (F) Bhat et al. (2013) (*$p = 0.0124$, unpaired t test).

(G) *AXL* expression is higher in the MES subtype (n = 18) compared with the IDH (n = 5), RTKI (n = 5), and RTKII (n = 28) subtypes, as determined by RNaseq data from individual patients (TCGA dataset, classification by Sturm et al., 2012). Error bars represent the minimum and maximum data points (*$p < 0.05$; unpaired t test).

(H) *AXL* is higher in the MES subtype (n = 55) compared with the classical (n = 42), PN (n = 31), and G-CIMP (n = 8) subtypes but not to the neural (n = 28) subtype, as determined by RNaseq data from individual patients (TCGA dataset) (*$p < 0.05$, **$p < 0.01$, ****$p < 0.0001$; unpaired t test). Error bars represent the minimum and maximum data points.
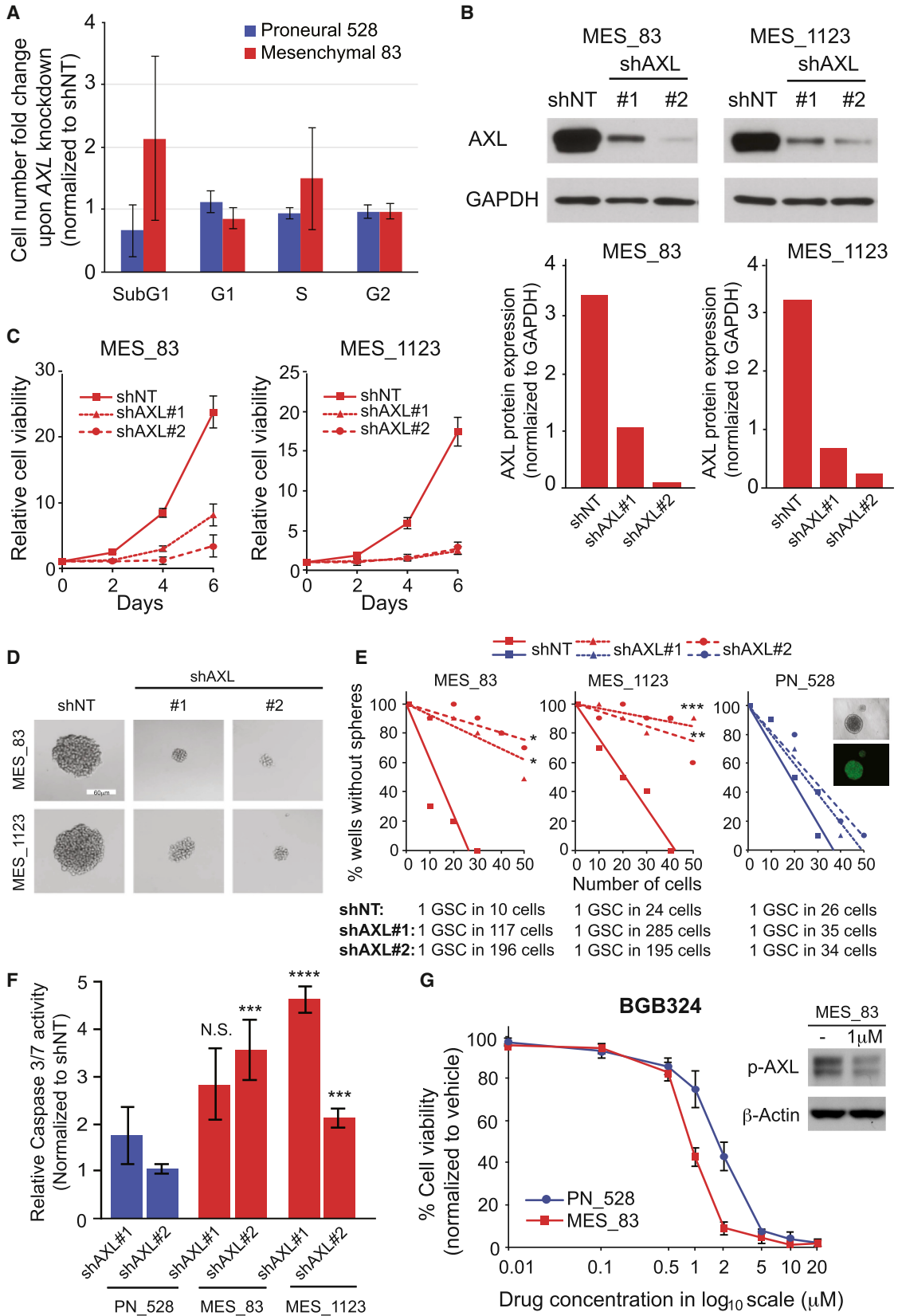
(legend on next page)

neurospheres (16wf) (Guvenc et al., 2013; Miyazaki et al., 2012; Nakano et al., 2011).

Lentivirus Production and Transduction

Screening of the kinase panel shRNA from The Mission RNAi library (Sigma-Aldrich) was performed in 96-well plates as previously described (Goidts et al., 2012). Briefly, DNA preparations were obtained using a large-scale plasmid purification kit (QIAGEN and Roche). HEK293T packaging cells were co-transfected with the pLKO.1 vector encoding the shRNA and the helper plasmids for virus production (psPAX2 and pMGD2), using Trans-IT (Mirus). Before transduction, spheres were dissociated mechanically (83 MES GSC) or with trypsin (528 PN GSC). Cells were seeded in 96-well plates at 10,000 cells per well in a final volume of 100 μl and transduced at a multiplicity of infection of 10. At 24 hr after transduction, medium was renewed upon plate centrifugation for 2 min at 800 rpm. Further details about the controls are available in the Supplemental Information.

The production of single shRNAs targeting *AXL* (shAXL#1: GCGGTCTGCATGAAGGAATTT, shAXL#2: GCTGTGAAGACGAT GAAGATT) was performed in 6-cm petri dishes. After 72 hr, produced lentiviruses were concentrated by ultracentrifugation of the HEK293T supernatant at 25,000 rpm.

High-Throughput FACS Analysis

Cell-cycle analysis was performed using a propidium iodide (PI) staining assay. Briefly, cells were fixed using 70% ethanol 5 days after viral transduction. After incubation at 4°C overnight, plates were centrifuged at 1,000 rpm for 5 min. Ethanol was removed, and 200-μl room temperature cell-cycle staining reagent (0.1% Triton X-100,PBS, 200-μg/ml DNase-free RNase, 250-μg/ml PI) was added. Cells were resuspended, and the plates were incubated at room temperature for 30 min, followed by cell-cycle analysis using a flow cytometer equipped with a high-throughput sampler. To minimize potential artifacts caused by edge effects, the outermost wells were not used.

Gene Expression Analysis

Gene expression data were downloaded from GEO datasets: Mao et al. (2013) (GSE 67089), Bhat et al. (2013) (GSE49009), De Bacco et al. (2012) (GSE36426), Sun et al. (2006) (GSE4290). R Bioconductor was used for the analysis of raw .cel files. The heatmap of transcriptomics analysis was made by Cluster and Treeview.

In Vitro Proliferation and Apoptosis Assay

After 83 and 1123 MES GSCs had been infected with *AXL* shRNA lentivirus for 5 days, 1,000 cells were seeded into wells of 96-well plates. AlamarBlue (Life Technologies) was used for the evaluation of cell number following the protocol provided by manufacturer at different time points (days 0, 2, 4, and 6). In order to measure apoptosis upon *AXL* silencing, 5,000 cells were seeded per well in a 96-well plate and transduced with shNT or shAXL. After 4 days, caspase 3 and 7 activities were measured using a Caspase-Glo 3/7 Assay (Promega), according to the manufacturer's instructions. BGB324 was used to treat cells at final concentrations of 0.01, 0.1, 0.5, 1, 2, 5, 10, and 20 μM. After dissociation into single-cell suspensions, 1,000 cells per well were seeded into 96-well plates. At 72 hr after treatment, cell viability was measured using AlamarBlue.

Limiting Dilution Neurosphere Formation Assay

After infection with shNT and shAXL lentivirus as described above, 83 and 1123 MES GSCs were seeded into 96-well plates at densities of 1, 10, 20, 30, 40, and 50 cells per well. Spheres with diameters >60 μm were counted at day 7 under an inverted microscope with a digital camera (Olympus). Extreme limiting dilution assay (ELDA) analysis were performed using the software available at http://bioinf.wehi.edu.au/software/elda/.

Western Blot Analysis

A detailed protocol can be found in the supplemental information. The membranes were treated with anti-AXL (Cell Signaling

---

Figure 4. AXL Is Required for the Growth and Clonogenicity of MES GSCs

(A) Average FC of cell number in different phases of the cell cycle upon *AXL* knockdown normalized to shNT. Error bars represent the SD from 5 independent shRNAs targeting *AXL*.

(B) Representative western blot results of shNT and shAXL samples from 83 and 1123 GSCs with GAPDH as a loading control (upper). AXL expression was quantified and normalized to GAPDH (lower).

(C) In vitro growth assay in 83 and 1123 MES GSCs transduced with shNT or two different shRNA targeting *AXL* (shAXL#1 and #2) measured at days 2, 4, and 6. Error bars represent the SD of three technical replicates.

(D) Representative pictures of GSCs cultivated as neurospheres transduced with shNT or *AXL* directed shAXL#1 or shAXL#2. Pictures were taken 5 days after transduction. Scale bar represents 60 μm.

(E) Limiting dilution neurosphere formation assay in MES (83 and 1123) and PN (528) GSCs. Cells were transduced with shNT or shAXL#1 or shAXL#2 in ten technical replicates. Readout was performed 12 days after transduction (*p < 0.5; **p < 0.01; ***p < 0.001; linear regression analysis). Stem cell frequency was calculated by ELDA analysis.

(F) Caspase activity assay of PN 528 GSCs and MES GSCs (83 and 1123) 4 days after transduction with shNT and shAXL#1 and shAXL#2. Results are normalized to shNT. Error bars represent the SD of three biological replicates. Significance was assessed by comparing the rate of caspase activity for each shRNA in the PN GSC line with the MES GSC lines (N.S. = not significant; ***p < 0.005; ****p < 0.001; paired t test).

(G) AXL inhibitor treatment effects on MES_83 and PN_528 GSC growth. Results were obtained 72 hr after BGB324 treatment at the indicated concentrations (IC$_{50}$ of 1.027 μM [MES_83] and 2.035 μM [PN_528]). Error bars represent the SD of three technical replicates. Western blot phospho-AXL expression in MES 83 GSCs with or without BGB324 treatment for 24 hr. β-Actin served as loading control.
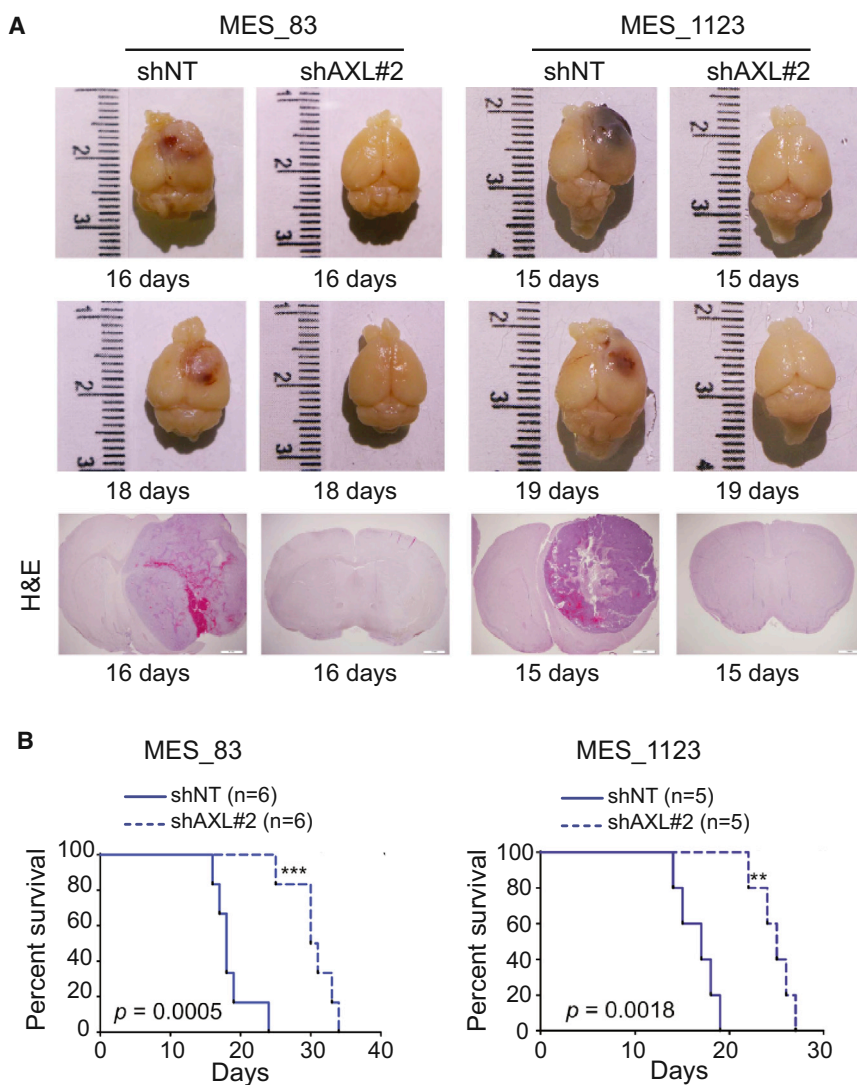
Figure 5. AXL Contributes to Tumor Propagation of MES GSCs

(A) Representative photographs of mouse brains injected with 83 and 1123 GSCs transduced with shNT or shAXL#2 and representative H&E staining of shNT and shAXL mouse xenografts at the indicated time points.

(B) Kaplan-Meier survival curves for mice injected with 83 and 1123 GSCs transduced with shNT (n = 6 and n = 5, respectively) and shAXL#2 (n = 6 and n = 5, respectively) (see also Figure S4).

#8661), anti-phospho-AXL (R&D AF2228), and anti-GAPDH antibodies (Abcam ab9482). Protein expression was visualized with Amersham ECL western blot system (GE Healthcare Life Sciences). GAPDH served as a loading control, and band intensity was quantified using Image J software.

RNA Extraction and qRT-PCR

Total RNA was prepared using RNeasy mini kit (QIAGEN) according to the manufacturer's instructions. A detailed protocol and primer sequences are listed in the Supplemental Information.

Immunohistochemistry

Immunohistochemistry (IHC) was carried out as previously described (Jijiwa et al., 2011). After perfusion with ice-cold PBS and 4% (wt/vol) paraformaldehyde (PFA), mice brains were fixed in 4% PFA for 24 hr and then transferred into 10% formalin. Tissue embedding and sectioning were performed at the Comparative

Pathology and Mouse Phenotyping Shared Resource of Ohio State University. The slides were treated with primary antibody overnight at 4°C and incubated with a horseradish peroxidase (HRP)-conjugated secondary antibody for 1 hr at room temperature. Slides incubated without primary antibodies served as negative controls. Chromogenic visualization followed using a DAB substrate kit (Vector), and nuclei were counterstained with hematoxylin.

Immunocytochemistry and Immunofluorescence

For immunocytochemistry, neurospheres were dissociated into single cells and seeded onto coverslips coated with 0.5% laminin (2×10^4 per well). After 24 hr, the cells were fixed with 4% (wt/vol) PFA, blocked with 1% BSA containing 0.3% Triton-X, and treated with primary antibody at 4°C overnight. The cells were then incubated with Alexa Flour 555-conjugated secondary antibody for 45 min at room temperature. Nuclei were counterstained
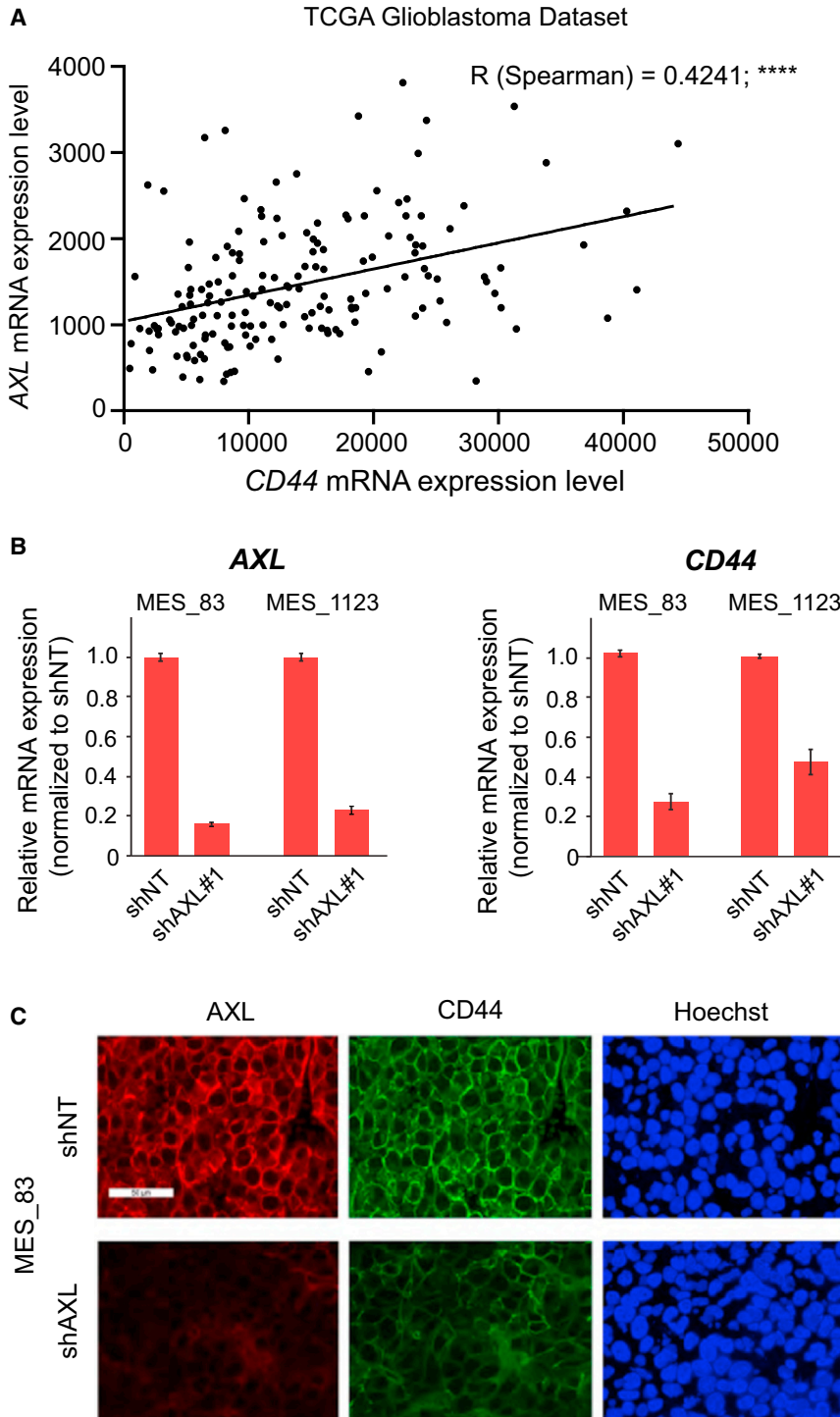
**Figure 6. AXL Expression Correlates with CD44**

(A) *AXL* mRNA expression significantly correlates with *CD44* mRNA expression. RNaseq data from n = 169 GBM patients are represented.

(B) Relative mRNA expression of *AXL* and *CD44* upon AXL knockdown. Data are normalized to shNT and are represented as mean of technical replicates ± SD.

(C) Immunofluorescent staining of AXL and CD44 on MES_83 GSCs in the mouse brain with (shAXL#2) or without (shNT) knockdown of AXL. Tumors were removed 24 days after injection (see also Figure S5). Scale bar represents 50 μm.

with Hoechst 35228, and the coverslips were mounted with anti-fade reagent (Life Technologies). Images were captured using a fluorescence upright microscope (Olympus DP71). Identical filters, objectives, and acquisition parameters were used for each experiment.

For immunofluorescence, mouse brains were fixed, embedded, and sectioned as described above. After blocking for 1 hr with 10% normal goat serum, the slides were co-incubated with rabbit anti-AXL (Cell Signaling, #8661) and mouse anti-CD44 antibody (Cell Signaling, #3570) overnight at 4°C and treated with
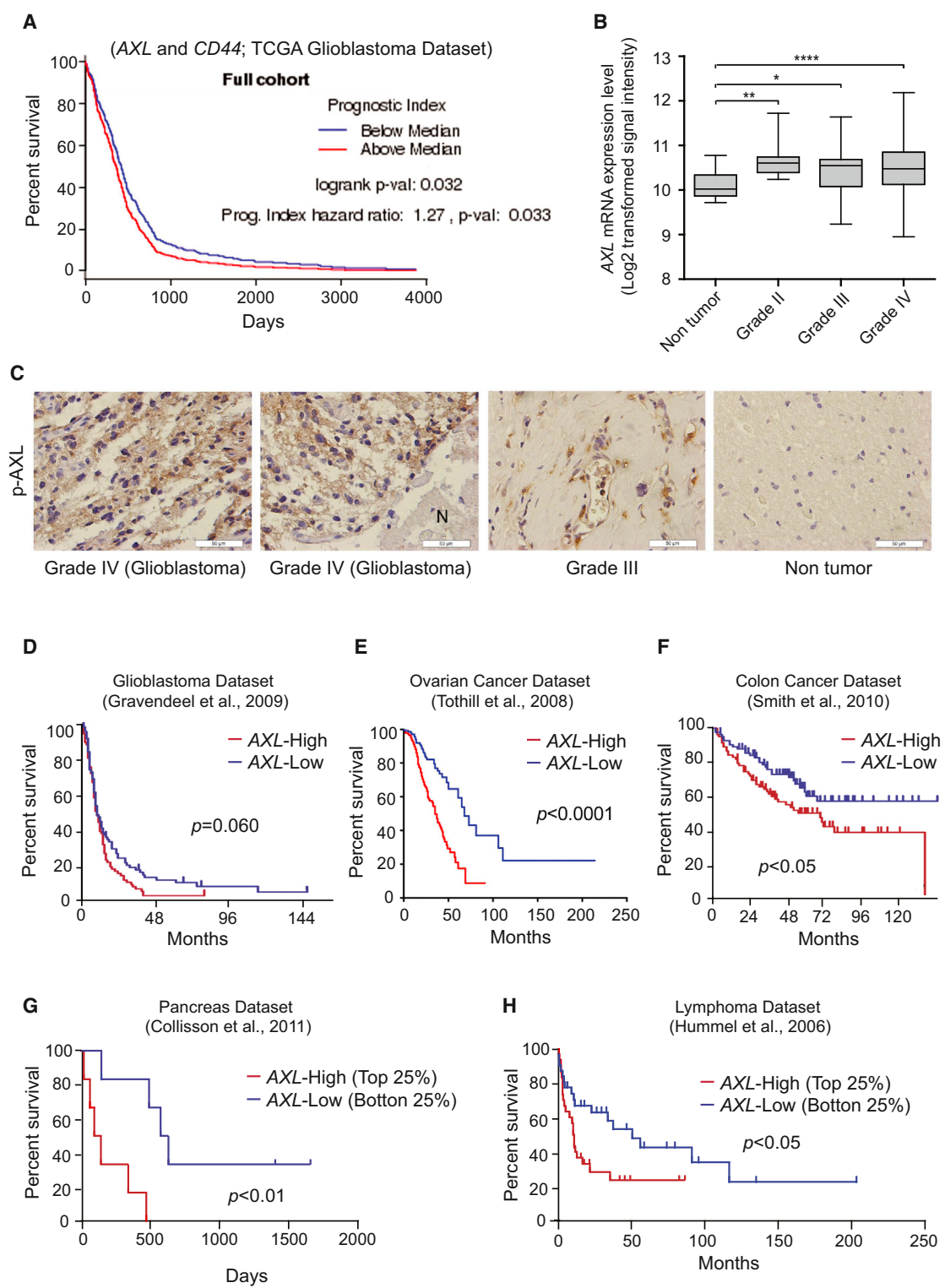
Figure 7. AXL Is Highly Expressed in Clinical High-Grade Glioma Tumors

(A) Survival analysis based on the impact of the multi-gene prognostic index. Affymetrix data generated by TCGA Research Network that are available at the TCGA data portal were used. Visualization of the data was performed using the GBM-BioDP (Celiku et al., 2014).

(B) *AXL* is more highly expressed in astrocytoma and GBM than in non-tumor tissue (Sun et al., 2006) (n = 23 non-tumor; n = 7 grade II; n = 19 grade III; n = 81 GBM). *p < 0.05, **p < 0.01, ****p < 0.0001 (Mann-Whitney test).

(legend continued on next page)

anti-mouse Alexa Fluor 488 (Cell Signaling) and anti-rabbit Alexa Fluor 555 (Cell Signaling) conjugated secondary antibodies for 1 hr at room temperature. Counterstaining was performed with Hoechst 35228 (Cell Signaling), and images were captured as described above.

In Vivo Tumor Propagation

Six-week-old nude mice were obtained from the animal research facilities of The Ohio State University. All animal experiments were carried out at The Ohio State University under an Institutional Animal Care and Use Committee (IACUC)-approved protocol according to NIH guidelines (IACUC Number: 2009A0241); 83 and 1123 MES GSC suspensions expressing shNT and shAXL#2 (1×10^4 cells in 2 μl of PBS) were injected into the brains of nude mice as previously described (Guvenc et al., 2013; Miyazaki et al., 2012; Nakano and Kornblum, 2009). Animals were monitored until the development of neuropathological symptoms.

Statistical Analysis

For analysis of FACS data, measurements with less than 2,000 cell counts were excluded. Measurements were standardized by the average of the non-target shRNA measurements separately for each plate. Ratios were log2 transformed to more closely follow a normal distribution. Relevant kinase directed shRNAs were identified using the empirical Bayes approach (Smyth, 2004) based on moderated t statistics as implemented in the Bioconductor package limma (Smyth, 2005). All p values were adjusted for multiple testing using Benjamini-Hochberg correction in order to control the false discovery rate. Adjusted p values below 0.05 were considered statistically significant. All analyses were carried out using software R 3.0.1. (RDC Team, 2011). A detailed method is described in the Supplemental Information.

Functional data were analyzed using Graphpad prism 6 and presented as mean ± SD. Statistical significance of Kaplan-Meier survival plot was determined by log-rank test; p < 0.05 was considered as statistically significant for all statistical methods.

SUPPLEMENTAL INFORMATION

Supplemental Information includes Supplemental Experimental Procedures and five figures and can be found with this article online at http://dx.doi.org/10.1016/j.stemcr.2015.03.005.

AUTHOR CONTRIBUTIONS

P.C. and E.P. designed experiments, performed experiments, and analyzed data. S.-H.K. performed experiments and analyzed data. D.T. and L.P. performed experiments. T.H. analyzed data. A.H. and P.L. wrote the manuscript. I.N. designed experiments, analyzed data, and wrote manuscript. V.G. designed experiments, performed experiments, analyzed data, and wrote the manuscript.

REFERENCES

Bhat, K.P., Balasubramaniyan, V., Vaillant, B., Ezhilarasan, R., Hummelink, K., Hollingsworth, F., Wani, K., Heathcock, L., James, J.D., Goodman, L.D., et al. (2013). Mesenchymal differentiation mediated by NF-κB promotes radiation resistance in glioblastoma. Cancer Cell 24, 331–346.

Brennan, C.W., Verhaak, R.G., McKenna, A., Campos, B., Noushmehr, H., Salama, S.R., Zheng, S., Chakravarty, D., Sanborn, J.Z., Berman, S.H., et al.; TCGA Research Network (2013). The somatic genomic landscape of glioblastoma. Cell 155, 462–477.

Celiku, O., Johnson, S., Zhao, S., Camphausen, K., and Shankavaram, U. (2014). Visualizing molecular profiles of glioblastoma with GBM-BioDP. PLoS ONE 9, e101239.

Choueiri, T.K., Vaishampayan, U., Rosenberg, J.E., Logan, T.F., Harzstark, A.L., Bukowski, R.M., Rini, B.I., Srinivas, S., Stein, M.N., Adams, L.M., et al. (2013). Phase II and biomarker study of the dual MET/VEGFR2 inhibitor foretinib in patients with papillary renal cell carcinoma. J. Clin. Oncol. 31, 181–186.

Collisson, E.A., Sadanandam, A., Olson, P., Gibb, W.J., Truitt, M., Gu, S., Cooc, J., Weinkle, J., Kim, G.E., Jakkula, L., et al. (2011). Subtypes of pancreatic ductal adenocarcinoma and their differing responses to therapy. Nat. Med. 17, 500–503.

De Bacco, F., Casanova, E., Medico, E., Pellegatta, S., Orzan, F., Albano, R., Luraghi, P., Reato, G., D'Ambrosio, A., Porrati, P., et al. (2012). The MET oncogene is a functional marker of a glioblastoma stem cell subtype. Cancer Res. 72, 4537–4550.

Druker, B.J., Sawyers, C.L., Kantarjian, H., Resta, D.J., Reese, S.F., Ford, J.M., Capdeville, R., and Talpaz, M. (2001). Activity of a

(C) Representative immunohistochemistry (ICH) staining of phospho-AXL in WHO grade IV (GBM), grade III and non-tumor samples. Scale bar represents 50 μm.
(D–H) Patient survival data based on *AXL* expression. (D) GBM dataset. The cutoff was based on the median, n = 156, p = 0.060 with log-rank test. (E) Ovarian cancer dataset through Oncomine. The cutoff was based on the median, n = 288, p < 0.0001 with log-rank test. (F) Poorly and moderately differentiated colon cancer samples. The cutoff was based on the median, n = 164, p < 0.05 with log-rank test. (G) Top and bottom 25% samples from the pancreatic ductal carcinoma dataset through Oncomine, n = 13, p < 0.01 with log-rank test. (H) Top and bottom 25% samples from the Burkitt's lymphoma dataset through Oncomine, n = 60, p < 0.05 with log-rank test.

specific inhibitor of the BCR-ABL tyrosine kinase in the blast crisis of chronic myeloid leukemia and acute lymphoblastic leukemia with the Philadelphia chromosome. N. Engl. J. Med. *344*, 1038–1042.

Ernst, A., Hofmann, S., Ahmadi, R., Becker, N., Korshunov, A., Engel, F., Hartmann, C., Felsberg, J., Sabel, M., Peterziel, H., et al. (2009). Genomic and expression profiling of glioblastoma stem cell-like spheroid cultures identifies novel tumor-relevant genes associated with survival. Clin. Cancer Res. *15*, 6541–6550.

Goidts, V., Bageritz, J., Puccio, L., Nakata, S., Zapatka, M., Barbus, S., Toedt, G., Campos, B., Korshunov, A., Momma, S., et al. (2012). RNAi screening in glioma stem-like cells identifies PFKFB4 as a key molecule important for cancer cell survival. Oncogene *31*, 3235–3243.

Gravendeel, L.A., Kouwenhoven, M.C., Gevaert, O., de Rooi, J.J., Stubbs, A.P., Duijm, J.E., Daemen, A., Bleeker, F.E., Bralten, L.B., Kloosterhof, N.K., et al. (2009). Intrinsic gene expression profiles of gliomas are a better predictor of survival than histology. Cancer Res. *69*, 9065–9072.

Gu, C., Banasavadi-Siddegowda, Y.K., Joshi, K., Nakamura, Y., Kurt, H., Gupta, S., and Nakano, I. (2013). Tumor-specific activation of the C-JUN/MELK pathway regulates glioma stem cell growth in a p53-dependent manner. Stem Cells *31*, 870–881.

Guvenc, H., Pavlyukov, M.S., Joshi, K., Kurt, H., Banasavadi-Siddegowda, Y.K., Mao, P., Hong, C., Yamada, R., Kwon, C.H., Bhasin, D., et al. (2013). Impairment of glioma stem cell survival and growth by a novel inhibitor for Survivin-Ran protein complex. Clin. Cancer Res. *19*, 631–642.

Hemmati, H.D., Nakano, I., Lazareff, J.A., Masterman-Smith, M., Geschwind, D.H., Bronner-Fraser, M., and Kornblum, H.I. (2003). Cancerous stem cells can arise from pediatric brain tumors. Proc. Natl. Acad. Sci. USA *100*, 15178–15183.

Holland, S.J., Pan, A., Franci, C., Hu, Y., Chang, B., Li, W., Duan, M., Torneros, A., Yu, J., Heckrodt, T.J., et al. (2010). R428, a selective small molecule inhibitor of Axl kinase, blocks tumor spread and prolongs survival in models of metastatic breast cancer. Cancer Res. *70*, 1544–1554.

Hummel, M., Bentink, S., Berger, H., Klapper, W., Wessendorf, S., Barth, T.F., Bernd, H.W., Cogliatti, S.B., Dierlamm, J., Feller, A.C., et al.; Molecular Mechanisms in Malignant Lymphomas Network Project of the Deutsche Krebshilfe (2006). A biologic definition of Burkitt's lymphoma from transcriptional and genomic profiling. N. Engl. J. Med. *354*, 2419–2430.

Janning, M., Ben-Batalla, I., and Loges, S. (2015). Axl inhibition: a potential road to a novel acute myeloid leukemia therapy? Expert Rev Hematol *8*, 135–138.

Jijiwa, M., Demir, H., Gupta, S., Leung, C., Joshi, K., Orozco, N., Huang, T., Yildiz, V.O., Shibahara, I., de Jesus, J.A., et al. (2011). CD44v6 regulates growth of brain tumor stem cells partially through the AKT-mediated pathway. PLoS ONE *6*, e24217.

Keating, A.K., Kim, G.K., Jones, A.E., Donson, A.M., Ware, K., Mulcahy, J.M., Salzberg, D.B., Foreman, N.K., Liang, X., Thorburn, A., and Graham, D.K. (2010). Inhibition of Mer and Axl receptor tyrosine kinases in astrocytoma cells leads to increased apoptosis and improved chemosensitivity. Mol. Cancer Ther. *9*, 1298–1307.

Knubel, K.H., Pernu, B.M., Sufit, A., Nelson, S., Pierce, A.M., and Keating, A.K. (2014). MerTK inhibition is a novel therapeutic approach for glioblastoma multiforme. Oncotarget *5*, 1338–1351.

Lee, J., Kotliarova, S., Kotliarov, Y., Li, A., Su, Q., Donin, N.M., Pastorino, S., Purow, B.W., Christopher, N., Zhang, W., et al. (2006). Tumor stem cells derived from glioblastomas cultured in bFGF and EGF more closely mirror the phenotype and genotype of primary tumors than do serum-cultured cell lines. Cancer Cell *9*, 391–403.

Linger, R.M., Keating, A.K., Earp, H.S., and Graham, D.K. (2008). TAM receptor tyrosine kinases: biologic functions, signaling, and potential therapeutic targeting in human cancer. Adv. Cancer Res. *100*, 35–83.

Liu, L., Greger, J., Shi, H., Liu, Y., Greshock, J., Annan, R., Halsey, W., Sathe, G.M., Martin, A.M., and Gilmer, T.M. (2009). Novel mechanism of lapatinib resistance in HER2-positive breast tumor cells: activation of AXL. Cancer Res. *69*, 6871–6878.

Mao, P., Joshi, K., Li, J., Kim, S.H., Li, P., Santana-Santos, L., Luthra, S., Chandran, U.R., Benos, P.V., Smith, L., et al. (2013). Mesenchymal glioma stem cells are maintained by activated glycolytic metabolism involving aldehyde dehydrogenase 1A3. Proc. Natl. Acad. Sci. USA *110*, 8644–8649.

Mellinghoff, I.K., Schultz, N., Mischel, P.S., and Cloughesy, T.F. (2012). Will kinase inhibitors make it as glioblastoma drugs? Curr. Top. Microbiol. Immunol. *355*, 135–169.

Miyazaki, T., Pan, Y., Joshi, K., Purohit, D., Hu, B., Demir, H., Mazumder, S., Okabe, S., Yamori, T., Viapiano, M., et al. (2012). Telomestatin impairs glioma stem cell survival and growth through the disruption of telomeric G-quadruplex and inhibition of the proto-oncogene, c-Myb. Clin. Cancer Res. *18*, 1268–1280.

Nakano, I., and Kornblum, H.I. (2009). Methods for analysis of brain tumor stem cell and neural stem cell self-renewal. Methods Mol. Biol. *568*, 37–56.

Nakano, I., Joshi, K., Visnyei, K., Hu, B., Watanabe, M., Lam, D., Wexler, E., Saigusa, K., Nakamura, Y., Laks, D.R., et al. (2011). Siomycin A targets brain tumor stem cells partially through a MELK-mediated pathway. Neuro-oncol. *13*, 622–634.

O'Bryan, J.P., Frye, R.A., Cogswell, P.C., Neubauer, A., Kitch, B., Prokop, C., Espinosa, R., 3rd, Le Beau, M.M., Earp, H.S., and Liu, E.T. (1991). axl, a transforming gene isolated from primary human myeloid leukemia cells, encodes a novel receptor tyrosine kinase. Mol. Cell. Biol. *11*, 5016–5031.

Patel, A.P., Tirosh, I., Trombetta, J.J., Shalek, A.K., Gillespie, S.M., Wakimoto, H., Cahill, D.P., Nahed, B.V., Curry, W.T., Martuza, R.L., et al. (2014). Single-cell RNA-seq highlights intratumoral heterogeneity in primary glioblastoma. Science *344*, 1396–1401.

Phillips, H.S., Kharbanda, S., Chen, R., Forrest, W.F., Soriano, R.H., Wu, T.D., Misra, A., Nigro, J.M., Colman, H., Soroceanu, L., et al. (2006). Molecular subclasses of high-grade glioma predict prognosis, delineate a pattern of disease progression, and resemble stages in neurogenesis. Cancer Cell *9*, 157–173.

Piao, Y., Liang, J., Holmes, L., Henry, V., Sulman, E., and de Groot, J.F. (2013). Acquired resistance to anti-VEGF therapy in glioblastoma is associated with a mesenchymal transition. Clin. Cancer Res. *19*, 4392–4403.

Qian, F., Engst, S., Yamaguchi, K., Yu, P., Won, K.A., Mock, L., Lou, T., Tan, J., Li, C., Tam, D., et al. (2009). Inhibition of tumor cell growth, invasion, and metastasis by EXEL-2880 (XL880, GSK1363089), a novel inhibitor of HGF and VEGF receptor tyrosine kinases. Cancer Res. 69, 8009–8016.

RDC Team. (2011). R: A Language and Environment for Statistical Computing (Vienna: R Foundation for Statistical Computing).

Shah, M.A., Wainberg, Z.A., Catenacci, D.V., Hochster, H.S., Ford, J., Kunz, P., Lee, F.C., Kallender, H., Cecchi, F., Rabe, D.C., et al. (2013). Phase II study evaluating 2 dosing schedules of oral foretinib (GSK1363089), cMET/VEGFR2 inhibitor, in patients with metastatic gastric cancer. PLoS ONE 8, e54014.

Singh, S.K., Hawkins, C., Clarke, I.D., Squire, J.A., Bayani, J., Hide, T., Henkelman, R.M., Cusimano, M.D., and Dirks, P.B. (2004). Identification of human brain tumour initiating cells. Nature 432, 396–401.

Smith, J.J., Deane, N.G., Wu, F., Merchant, N.B., Zhang, B., Jiang, A., Lu, P., Johnson, J.C., Schmidt, C., Bailey, C.E., et al. (2010). Experimentally derived metastasis gene expression profile predicts recurrence and death in patients with colon cancer. Gastroenterology 138, 958–968.

Smyth, G.K. (2004). Linear models and empirical bayes methods for assessing differential expression in microarray experiments. Stat. Appl. Genet. Mol. Biol. 3, e3.

Smyth, G.K. (2005). Limma: Linear Models for Microarray Data (New York: Springer).

Stupp, R., Hegi, M.E., Mason, W.P., van den Bent, M.J., Taphoorn, M.J., Janzer, R.C., Ludwin, S.K., Allgeier, A., Fisher, B., Belanger, K., et al.; European Organisation for Research and Treatment of Cancer Brain Tumour and Radiation Oncology Groups; National Cancer Institute of Canada Clinical Trials Group (2009). Effects of radiotherapy with concomitant and adjuvant temozolomide versus radiotherapy alone on survival in glioblastoma in a randomised phase III study: 5-year analysis of the EORTC-NCIC trial. Lancet Oncol. 10, 459–466.

Sturm, D., Witt, H., Hovestadt, V., Khuong-Quang, D.A., Jones, D.T., Konermann, C., Pfaff, E., Tönjes, M., Sill, M., Bender, S., et al. (2012). Hotspot mutations in H3F3A and IDH1 define distinct epigenetic and biological subgroups of glioblastoma. Cancer Cell 22, 425–437.

Sun, L., Hui, A.M., Su, Q., Vortmeyer, A., Kotliarov, Y., Pastorino, S., Passaniti, A., Menon, J., Walling, J., Bailey, R., et al. (2006). Neuronal and glioma-derived stem cell factor induces angiogenesis within the brain. Cancer Cell 9, 287–300.

Tothill, R.W., Tinker, A.V., George, J., Brown, R., Fox, S.B., Lade, S., Johnson, D.S., Trivett, M.K., Etemadmoghadam, D., Locandro, B., et al.; Australian Ovarian Cancer Study Group (2008). Novel molecular subtypes of serous and endometrioid ovarian cancer linked to clinical outcome. Clin. Cancer Res. 14, 5198–5208.

Vajkoczy, P., Knyazev, P., Kunkel, A., Capelle, H.H., Behrndt, S., von Tengg-Kobligk, H., Kiessling, F., Eichelsbacher, U., Essig, M., Read, T.A., et al. (2006). Dominant-negative inhibition of the Axl receptor tyrosine kinase suppresses brain tumor cell growth and invasion and prolongs survival. Proc. Natl. Acad. Sci. USA 103, 5799–5804.

Verhaak, R.G., Hoadley, K.A., Purdom, E., Wang, V., Qi, Y., Wilkerson, M.D., Miller, C.R., Ding, L., Golub, T., Mesirov, J.P., et al.; Cancer Genome Atlas Research Network (2010). Integrated genomic analysis identifies clinically relevant subtypes of glioblastoma characterized by abnormalities in PDGFRA, IDH1, EGFR, and NF1. Cancer Cell 17, 98–110.

Vuoriluoto, K., Haugen, H., Kiviluoto, S., Mpindi, J.P., Nevo, J., Gjerdrum, C., Tiron, C., Lorens, J.B., and Ivaska, J. (2011). Vimentin regulates EMT induction by Slug and oncogenic H-Ras and migration by governing Axl expression in breast cancer. Oncogene 30, 1436–1448.

Zhang, J., Yang, P.L., and Gray, N.S. (2009). Targeting cancer with small molecule kinase inhibitors. Nat. Rev. Cancer 9, 28–39.

Zhang, Z., Lee, J.C., Lin, L., Olivas, V., Au, V., LaFramboise, T., Abdel-Rahman, M., Wang, X., Levine, A.D., Rho, J.K., et al. (2012). Activation of the AXL kinase causes resistance to EGFR-targeted therapy in lung cancer. Nat. Genet. 44, 852–860.

Kinome-wide shRNA Screen Identifies the Receptor Tyrosine Kinase *AXL* as a Key Regulator for Mesenchymal Glioblastoma Stem-like Cells

Peng Cheng, Emma Phillips, Sung-Hak Kim, David Taylor, Thomas Hielscher, Laura Puccio, Anita Hjelmeland, Peter Lichter, Ichiro Nakano, and Violaine Goidts
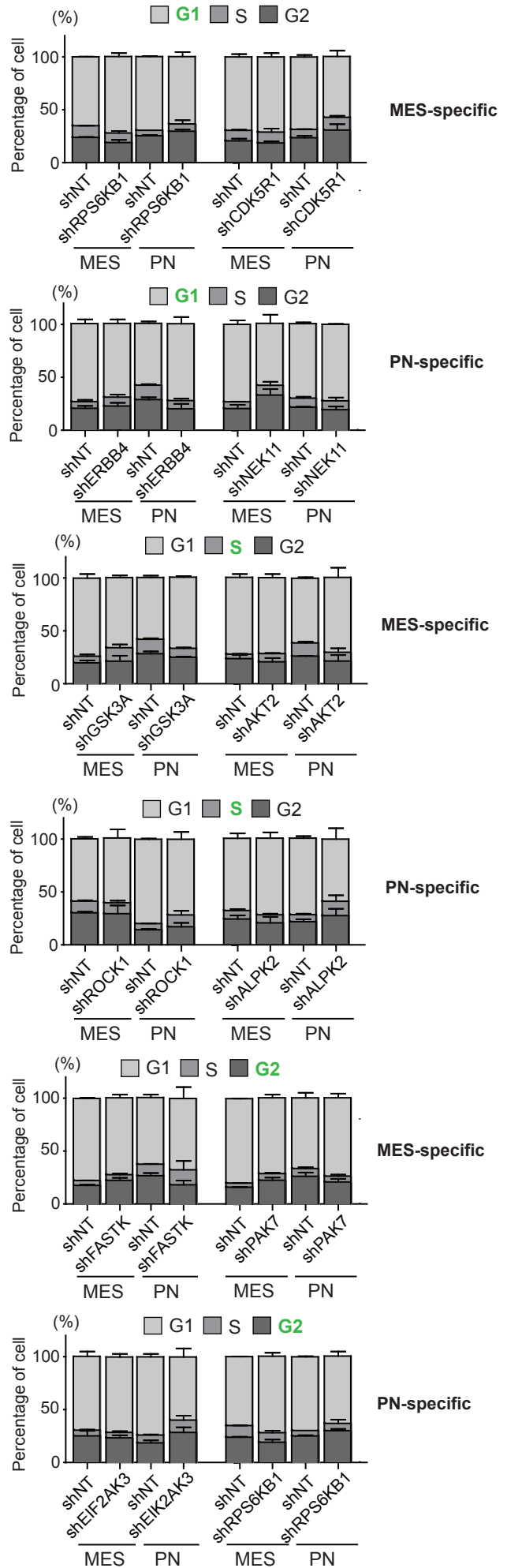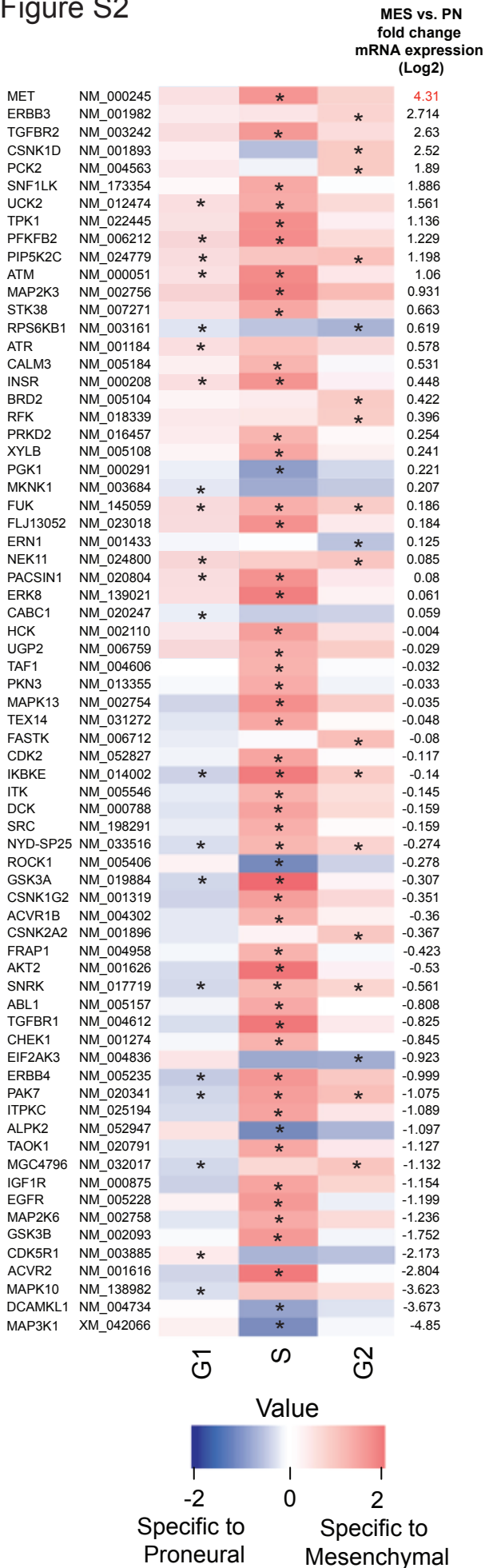
Figure S1

A

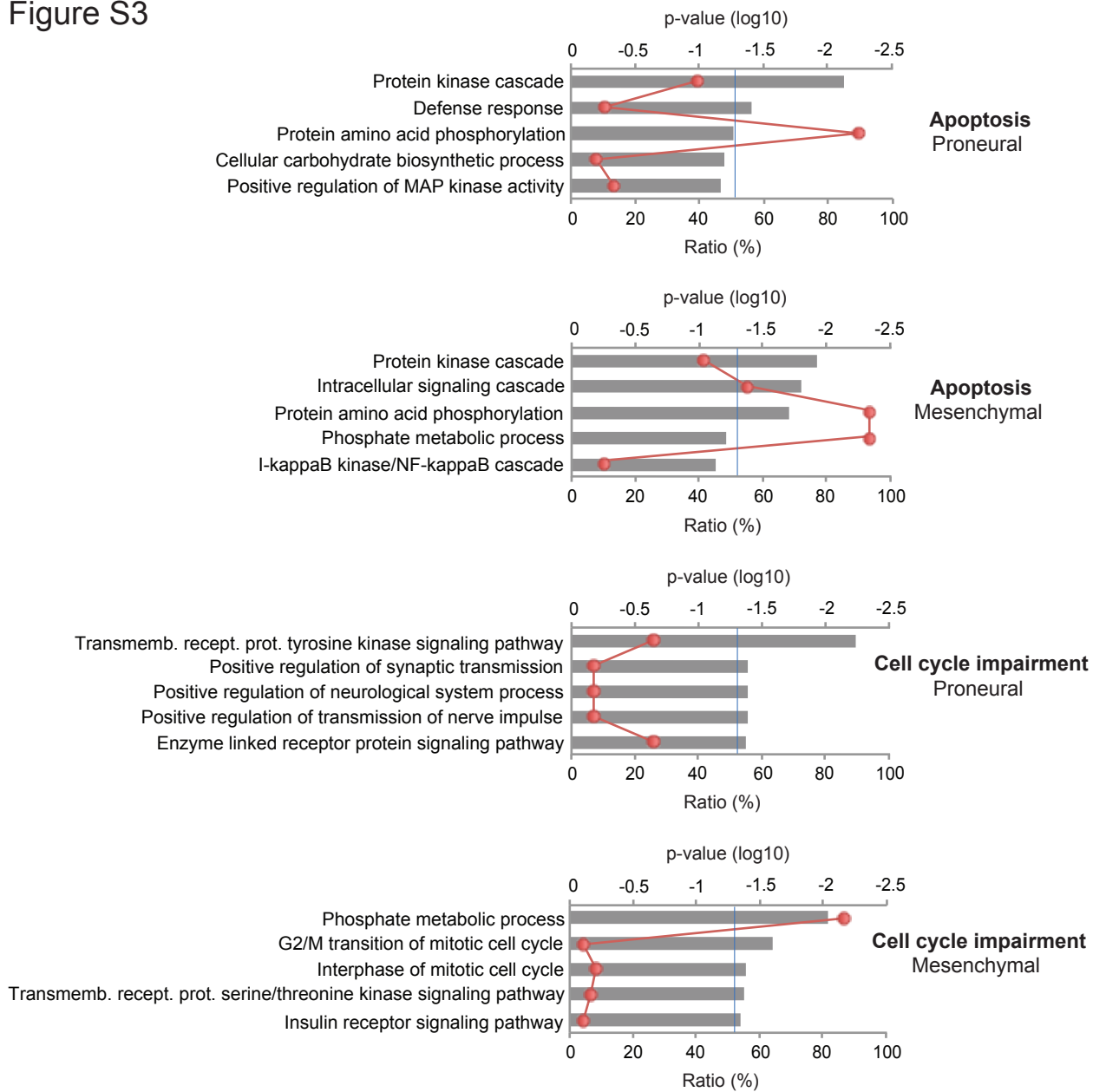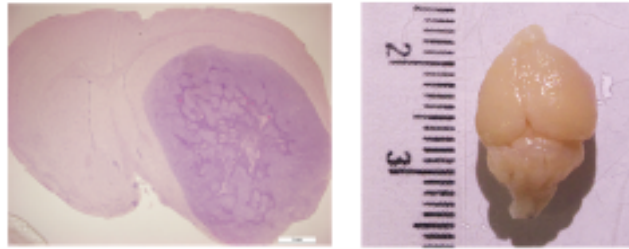| Gene	Accession	SubG1
FYN	NM_002037	*
RIPK3	NM_006871	*
RET	NM_020629	*
LOC340371	NM_178564	*
ICK	NM_014920	*
MAP2K1	NM_002755	*
PIM2	NM_006875	*

B

Gene	Accession	G1	S	G2
EGFR	NM_005228			*
CARKL	NM_013276		*	
EPHA5	NM_004439		*	
MAP4K2	NM_004579		*	
NTRK3	NM_002530		*	
CKM	NM_001824		*	
LYN	NM_002350		*	
EPHA2	NM_004431		*	
NPR1	NM_000906		*	
TESK1	NM_006285		*	
TTK	NM_003318		*	
FRK	NM_002031		*	
DAPK2	NM_014326			*

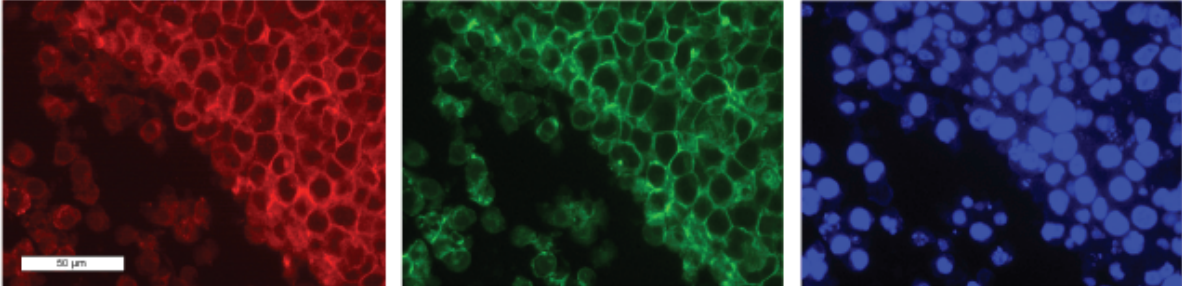Value

0 1 2 3 4

Figure S2

Figure S3

Figure S4

MES_83
shAXL#2

30 days

Figure S5

AXL	CD44	Hoechst

Supplementary Figure legends

Figure S1: Knockdown of a subset of kinases decreases viability and alters cell cycle of both MES and PN GSCs. Related to Figure 1

(A) Kinases that induce a significant level of cell death (*: p<0.05) in MES and PN GSCs when targeted with shRNA. The color code represents the fold increase of SubG1 phase cells after knockdown of the indicated gene compared to cells transduced with a non-targeting shRNA (shNT).

(B) Kinases that significantly alter the cell cycle in MES and PN GSCs (*. p<0.05) when targeted with shRNA. The color code represents the fold increase of cell numbers in the respective cell cycle phases compared to cells transduced with shNT. Stacked bar charts on the right panels represent the percentage of cells in the different phases of the cell cycle in MES and PN GSCs for the top two genes in each of the indicated cell cycle phases, as determined by FACS analysis of propidium iodide DNA staining. The average of the shNT used for normalization and the shRNAs targeting the indicated gene are shown. Error bars represent the standard deviation.

Figure S2: Knockdown of a subset of kinases differentially alters cell cycle in MES or PN GSCs. Related to Figure 2

(A) List of kinases that significantly (*: p<0.05) impair the cell cycle in MES GSCs (blue) or in PN GSCs (red) when targeted with shRNA. Data were normalized to the respective shNT. mRNA expression fold change between PN and MES GSCs is

indicated on the right side of the heatmap.

(B) Stacked bar charts depicting cell percentage of the top two genes in each cell cycle phase that when targeted with shRNA significantly impair the cell cycle. Average of the shNT used for normalization and the shRNAs targeting the indicated gene are shown. Error bars represent the standard deviation.

Figure S3: Gene ontology analysis using the DAVID tool of the candidate genes that impair MES or PN viability. Related to Figure 2

Kinases whose silencing increases SubG1 phases (described as apoptosis kinases) were separated from those that impair G1, S or G2 phases (described as proliferation impairing kinases). The human kinome was used as background to ensure statistical correctness.

Figure S4: Representative photographs of mice brains. Related to Figure 5

Animals were injected with 83 GSCs transduced with shAXL#2 and representative H&E staining of shAXL mouse xenografts, 30 days after transplantation, is shown.

Figure S5: Staining of AXL and CD44. Related to Figure 6

Staining was perfomed on a mouse brain tumor sample close to a necrotic area (83 GSCs). Scale bar: 50 µm.

Materials and methods

Lentiviral Production and Transduction

To assess transduction efficiency, cells on each plate were infected with lentivirus expressing green fluorescent protein (GFP). Transduction was deemed efficient if >70% cells were GFP-expressing. To reduce any position effects, the 3-5 shRNAs targeting each kinase where divided onto two plates and each plate included three replicates of a non-targeting shRNA (shNT). Measurements were standardized by the average of the shNT measurements separately for each plate. The titer was measured using lentiviral particles that contained the pLKO.1 vector expressing GFP and ranged from 2×10^6 to 4×10^6 Transduction Units/ml. Transductions were performed at the multiplicity of infection (MOI) of 10.

Reagents and Antibodies

The following primary antibodies and reagents were used in this study: EGF (Peprotech); bFGF (Peprotech); B27 (invitrogen); Heprin (Sigma); DMEM-F12 (Gibco, 10565-018); anti-AXL (Cell signaling, #8661) for immunocytochemistry, immunoflurescence and Western blot, anti-phospho-AXL (R&D AF2228) for immunocytochemistry, immunohistochemistry and Western blot; anti-GAPDH (Abcam, ab9482) for Western blot; anti-CD44 (Cell Signaling #3570) for immunofluorescence and (Miltenyl Biotec #130-090-854) for FACS; and anti-CD133 (Biolegend #103016) for FACS. Fetal bovine serum (Gibco, 10082-147); Albumin from bovine serum (Sigma, A2153); Accutase solution (Sigma, A6964-100); alamar

Blue (invitrogen, DAL1100); RIPA buffer (Sigma, R0278-50ml); Phophatase inhibitor cocktail (Sigma, P0044-5ml); Protease inhibitor cocktail (P8340); Bradford (BIO-RAD, 500-0006); BSA used in Bradford assay (BioLabs, B9001S); PageRuler plus prestained protein (Thermo scientific, 26619);. iScript Reverse Transcription supermix for RT-qPCR (Bio-rad, 170-8841); Caspase-Glo®3/7 Assay (Promega).

Western blot analysis

The cell lysates were prepared in RIPA buffer containing protease and phosphatase inhibitor cocktail (Sigma Aldrich) on ice. The sample protein concentrations were determined by the Bradford method. Equal amounts of protein lysates (10 μg/lane) were fractionated on NuPAGE Novex 4-12% Bis-Tris Protein gel (Invitrogen) and transferred to a PVDF membrane (Invitrogen). Subsequently, the membranes were blocked with 5% skimmed milk for 1 h and then treated with the relevant antibody at 4°C overnight. Protein expression was visualized with Amersham ECL Western Blot System (GE Healthcare Life Sciences). GAPDH served as a loading control.

Quantitative RT-PCR

Total RNA was prepared using a RNeasy mini kit (Qiagen) according to the manufacturer's instructions. RNA concentration was determined using a Nanodrop 2000 (Thermo scientific). RNA integrity was examined with an Agilent 2100 Bioanalyzer. For reverse transcription, the average RNA integrity number (RIN) was larger than 9.0. cDNA was synthesized by using iScript reverse transcription

supermix for RT-qPCR (Bio-rad) according to the manufacturer's protocol.

Quantitative RT-PCR was performed using a StepOnePlus real-time PCR system

with a SYBR Select Master Mix (Applied Biosystems). GAPDH was used as an

internal control. The following cycles were performed during DNA amplification: 94°C

for 2 min, 50 cycles of 94°C (30 s), 60°C (30 s), and 72°C (40 s). The primer

sequences for qPCR were as follows:

AXL forward: GTTTGGAGCTGTGATGGAAGGC;

AXL Reverse: CGCTTCACTCAGGAAATCCTCC (Gioia et al., 2011);

CD44 forward: CCCAGATGGAGAAAGCTCTG;

CD44 reverse: ACTTGGCTTTCTGTCCTCCA;

CD133 Forward: ACTCCCATAAAGCTGGACCCC;

CD133 Reverse: TCAATTTTGGATTCATATGCCTT;

GAPDH forward: GAAGGTGAAGGTCGGAGTCA;

GAPDH reverse: TTGAGGTCAATGAAGGGGTC.

Relative quantitation of cDNAs to *GAPDH* was determined by $2^{-\Delta\Delta Ct}$ method.

Statistical analysis

For analysis of FACS data, measurements with less than 2000 cell counts were

excluded. Measurements were standardized by the average of the non-target shRNA

measurements separately for each plate. Ratios were log2 transformed to more

closely follow a normal distribution. Relevant kinase directed shRNAs were identified

using the empirical Bayes approach (Smyth, 2004) based on moderated t-statistics

as implemented in the Bioconductor package limma (Smyth, 2005). Kinase directed shRNAs with differential activity between cell lines were identified for each cycle phase separately using one-sided p-values and a fold change (FC) threshold of the median FC plus two median absolute deviations. shRNAs showing an equivalent increase of cell number in the respective cell cycle phase in both cell lines were defined based on the following criteria: increase across cell lines was determined as for individual cell lines but based on shRNAs from both cell lines pooled using one-sided p-values and a FC threshold. The two-sided 90 % confidence interval for the difference between both cell lines was computed. Confidence limits had to fall within pre-specified boundaries in order to establish equivalence. Boundaries were defined in terms of acceptable absolute FC. Since magnitude and variability of cell number levels were very different for each cycle phase, different equivalence boundaries (FC 1.1 to 1.6) were applied for each phase. All p-values were adjusted for multiple testing using Benjamini-Hochberg correction in order to control the false discovery rate. Adjusted p-values below 0.05 were considered statistically significant. All analyses were carried out using software R 3.0.1. (Team, 2011).

MACS Cell Separation

PN_528 GSCs were separated according to their level of CD133 expression by MACS according to manufacturer's instruction. In brief, single cell suspensions were prepared with Accutase (Life technology). After 30 mins incubation with CD133 MicroBeads (Miltenyi Biotec) at 4°C, cells were added on LS columns (Miltenyi

Biotec) and placed in a MidiMACS separator. The flow-though cells were collected

as CD133 low cells. The cell fraction retained in the column was eluted as CD133

high cells.

REFERENCES

Gioia, R., Leroy, C., Drullion, C., Lagarde, V., Etienne, G., Dulucq, S., Lippert, E., Roche, S., Mahon, F.X., and Pasquet, J.M. (2011). Quantitative phosphoproteomics revealed interplay between Syk and Lyn in the resistance to nilotinib in chronic myeloid leukemia cells. Blood *118*, 2211-2221.

Smyth, G.K. (2004). Linear models and empirical bayes methods for assessing differential expression in microarray experiments. Statistical applications in genetics and molecular biology *3*, Article3.

Smyth, G.K. (2005). Limma: linear models for microarray data (New York: Springer).

Team, R.D.C. (2011). R: A language and environment for statistical computing. (Vienna, Austria: R Foundation for Statistical Computing).